II.1.3 Micro and Nano Scale Electrochemistry: Application to Fuel Cells

Investigators
Fritz B. Prinz, Professor, Mechanical Engineering, Materials Science and Engineering; Ryan O'Hayre, Minhwan Lee, Graduate Researchers

Introduction

Fuel cells offer the tantalizing promise of cleaner electricity with less impact on the environment than traditional energy conversion technologies. This is because fuel cells are direct electrochemical energy conversion devices. In other words, they convert chemical energy, in the form of a fuel and oxidant, directly into electrical energy. Contrast this to combustion engines, which first convert chemical energy into heat, heat into mechanical energy, and finally mechanical energy into electricity.

Widespread fuel cell viability will not occur without further technological breakthroughs. The emerging domain of nanoscience and technology may provide solutions. As identified in a U.S. Government report[1] on basic research needs for the hydrogen economy, nanoscience introduces powerful and virtually untapped new dimensions to fuel cell research.

Why should nanoscience be so beneficial to fuel cells? The answer comes from a deeper understanding of the fundamental principles involved in the electrochemical generation of electricity. Fuel cells produce electricity by converting a primary energy source (a fuel) into a flow of electrons. This conversion necessarily involves some sort of energy transfer step, where the energy from the source is passed along to the electrons constituting the electric current. This transfer has some finite rate and must occur at an interface or reaction surface. Thus, the amount of electricity produced scales with the amount of reaction surface area or interfacial area available for the energy transfer. Larger surface areas translate into improved performance. Unsurprisingly, then, the desire for large surface areas has led to a focus on nano-materials. A cube of material measuring 1 nm per side has 10^6 times greater surface to volume ratio compared to a cube of material measuring 1 mm per side. In addition, to increasing the 'outside' surface area of a particle by decreasing its dimensions one can also increase 'internal' surface area by introducing atomic defects such as dislocations to enhance species diffusivity and chemical reactivity.

Despite recent *technological* successes wrought by the clever incorporation of nano-structured materials in fuel cells, we are still far away from possessing a solid *scientific* understanding of what is really going on at the nano-scale. Many critical questions remain. For example:

- What are the characteristic dimensions over which energy transfer or charge transfer reactions can effectively occur?
- Is there such a thing as too small? If the periodicity of a nano-structured interface is smaller than the characteristic energy transfer dimension, the answer may be yes.

- How exactly do kinetic properties scale at small dimensions? Is there more than simple surface area scaling at work?

Studying the kinetic scaling behavior of nano-structured systems can be quite complicated. In fuel cell systems, for example, it has long been believed that the oxygen reduction reaction (ORR) can only occur at confined spatial regions, called "triple phase boundaries" (TPB's) where the electrolyte, gas, and electrically connected catalyst particles contact. However, the reaction-zone structure of a state of the art fuel cell is complex, consisting of a porous, heterogeneous mixture of conductive carbon powders and platinum particles, often mixed with a solid polymer electrolyte binder. Due to this complexity, the true amount of TPB in a fuel cell is difficult, if not impossible, to determine. Thus, the relationship between catalyst microstructure (ie, TPB geometry) and fuel cell performance is still unclear.

In order to begin answering some of these questions, this research pioneers several novel micro and nano-scale electrochemical techniques, which are used to study fuel cells at the sub-micron length scale. As a first approach, we have developed a technique that employs platinum microelectrodes to examine the TPB properties of polymer electrolyte fuel cells. By constructing reproducible, geometrically simple, well-defined electrocatalyst structures of various sizes, a relationship between electrocatalyst geometry and electrochemical behavior is clearly delineated. This study provides perhaps the most direct experimental validation to date of the TPB theory.

Extending our characterization ability to the nano-scale, a second technique, called AFM impedance imaging is also developed. The AFM impedance imaging technique allows highly localized measurements of electrochemical properties to be acquired across sample surfaces.

While the techniques presented in this report have been successfully employed to study the electrochemical behavior of fuel cells, characterizing and understanding nano-structures is a challenge that extends far beyond the fuel cell realm. Many other devices, such as solar cells, sensors, and thermoelectric converters also benefit from nano-structured materials. The parallels between these systems and fuel cells make them highly amenable to the same type of nanometer scale visualization and measurement techniques, offering rich opportunities for further research.

Background

The O_2/Nafion/Pt Triple Phase Boundary

The idea of the *triple phase boundary* (TPB) is extensively employed in the fuel cell literature, especially with respect to solid oxide fuel cells (SOFC's) and polymer electrolyte membrane fuel cells (PEMFC's). The TPB concept holds that hydrogen oxidation reaction (HOR) and the oxygen reduction reaction (ORR) can only occur at confined spatial sites, called "triple phase boundaries" (TPB's) where electrolyte, gas, and electrically connected catalyst regions contact. A simplified schematic of the TPB is shown in Fig.1. The reaction kinetics (especially the ORR kinetics) often present a significant limitation to fuel cell performance. Therefore, understanding, characterizing,

and optimizing the TPB content in fuel cells provides excellent opportunities for performance enhancement.

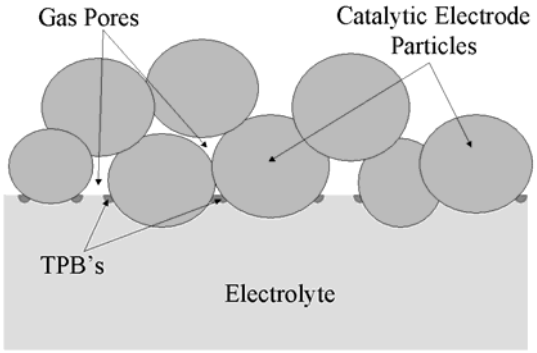

Figure 1: A simplified schematic diagram of the electrode/electolyte interface in a fuel cell, illustrating the triple phase boundary reaction zones where the catalytically active electrode particles, electrolyte phase, and gas pores intersect.

On the technology side, efforts to increase the amount of TPB in technological fuel cells with nano-structured catalyst-layers have proven highly successful. By employing nano-scale composites of catalyst material, conductive support, solid-electrolyte, and gas pore space, investigators have been able to dramatically increase the amount of TPB, thus improving kinetic performance.[2,3]

From a scientific perspective, recent efforts have been made to more clearly delineate the nature and properties of the TPB. Most of this work has been focused on SOFC's[4-8], with very few studies directed towards PEMFC's[9]. However, in all cases, there is a growing realization that the simple concept of the TPB as a singularity is unrealistic; rather, it should be thought of as a "zone", whose width, properties, and behavior depend on a complex interplay between coupled reaction and diffusion processes.

AFM Impedance Imaging

An ultimate tool for the rapid development and understanding of fuel cells and other energy conversion devices would be an imaging system that allows researchers to visualize the fundamental physical processes at work in the conversion of energy at the micro or nano scale. The development of such a tool embodies a major part of our research, and we report on steps towards this goal with the design and demonstration of an AFM impedance imaging system. The AFM impedance-imaging system permits spatially resolved electrochemical studies at the nanometer scale. First validated on simple test devices, the AFM technique is then applied to investigate sub-micron details of Nafion fuel cell electrolyte films and nano-scale platinum catalysts. The impedance imaging technique makes use of the scanning capabilities of the AFM to acquire 2-dimensional *images* of impedance across sample surfaces. While the potential of the system is demonstrated by application to electro ceramics and fuel cell systems, it is expected that nanometer scale visualization and measurement of impedance will be valuable for a wide variety of materials investigations, including solid electrolytes, semiconductors, solar cells, electro ceramics, coatings and corrosion research, and Li-ion battery and fuel cell systems.

Impedance spectroscopy (IS) is a key characterization tool in the research and development of diverse materials systems. In fuel cell and battery research, it has been used to distinguish between various sources of cell loss; for example ohmic losses in the electrodes and electrolyte, activation overpotentials due to reaction kinetics, and mass transport effects. While these measurements resolve electrochemical phenomena *mechanistically*, they cannot resolve the phenomena *spatially*. In other words, standard IS measurements produce bulk, or system averaged results.

Recently, several spatially resolved impedance techniques have been developed. Fleig et al.[10,11] have used patterned arrays of microelectrodes to acquire spatially resolved impedance data from polycrystalline ceramics with a lateral resolution of 15 to 20 μm. Issacs et al. and others[12-14] have demonstrated localized electrochemical impedance spectroscopy (LEIS) methods (now commercialized) that function in an aqueous electrolyte and are capable of acquiring impedance data with a resolution of about 30 μm. Most recently, Pilaski et al.[15] have developed a scanned technique based on a capillary liquid-electrolyte droplet cell with an apparent resolution of around 100 μm.

In contrast to these methods, the atomic force microscope (AFM) impedance imaging technique introduced in this report leverages the capabilities of an AFM to acquire impedance images with sub 100 nm resolution. Furthermore, the technique is designed to measure all solid-state materials systems. The system is constructed from a commercially available AFM coupled to impedance measurement hardware (Fig. 2a). The AFM tip, which must be conductive, serves as the probe electrode for the IS measurements. Successive measurements across a sample surface are obtained by moving the AFM tip. Due to the time requirements for impedance acquisition, measurements are currently obtained in a point-by-point fashion rather than in a continuous scanning manner. Single frequency or complete impedance spectra can be obtained during the scans. Custom developed software automates the communication and synchronization between the hardware systems.

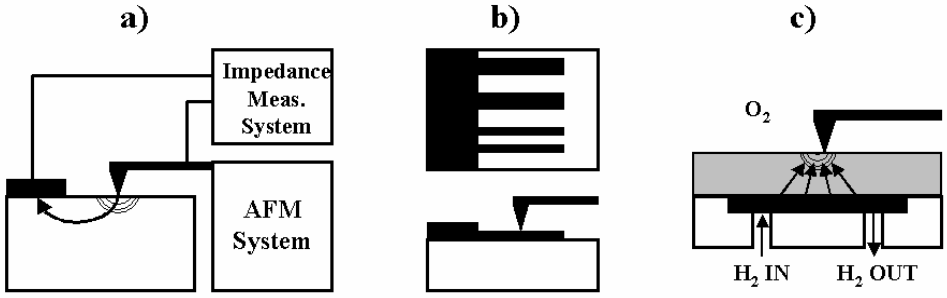

Figure 2: Schematics of the experimental configurations used in this study for AFM impedance imaging. **a)** General concept of AFM impedance imaging. Impedance is measured between a local probe (the AFM tip) and a bulk electrode. A significant spreading resistance contribution at the AFM tip/sample contact point ensures local characterization. (Shown schematically by the hemispherical lines.) **b)** Experimental configuration for the Au/Si_3N_4 test structures. The gold lines (black) are connected to the bulk electrode. If the AFM tip scans over the gold regions, an ohmic response should be obtained. **c)** Configuration for the Nafion characterization experiment. The impedance is

measured between an AFM tip on the Nafion top surface and a bulk bottom electrode (a reversible hydrogen electrode) which is hermetically sealed and supplied with hydrogen gas.

AFM electrical property measurements are not new. Scanning spreading resistance microscopy[16-18] (SSRM), conductive or current sensing AFM[19-21] (C-AFM), and tunneling-AFM[22,23] (TUNA) allow DC-characterization of materials. Other techniques make use of the long-range electrostatic forces between a sample and a conductive non-contact AFM tip to extract surface potential images[24,25] (scanning surface potential microscopy, SSPM) or capacitive information on semiconductor oxide surfaces[26-28] (scanning capacitance microscopy, SCM). Layson et al.[29] have obtained AC impedance data on poly(ethylene) oxide films directly through a conductive AFM tip at individual points on the film surface, but do not report impedance imaging. Recently, Kalinin and Bonnell[30,31] have reported a scanning impedance microscopy technique (SIM) that detects the phase change in a conductive non-contact cantilever as a lateral bias is applied to a sample of interest. This technique in combination with SSPM, is shown to be useful for the determination of AC transport properties across lateral interfaces. In the SIM technique, the voltage perturbation is not applied through the tip, but rather between macroscopic electrodes on the substrate. Shao, Kalinin, and Bonnell[32] have even more recently reported a contact version of SIM, using a similar technique to acquire localized impedance that we report here. Our contribution represents a significant elaboration on the details, capabilities, and limitations of the AFM impedance imaging technique, as well as an extension of the technique to the electrochemical and ionic domain.

Results

The Oxygen/Nafion/Pt Triple Phase Boundary

As detailed in the introduction and background sections to this report, there is a significant correlation between catalyst microstructure and performance in fuel cells. Specifically, it has been theorized that fuel cell performance depends strongly on the triple phase boundaries (TPB's) for the fuel cell reaction.

While many researchers have *theorized* on the existence and the importance of TPBs in fuel cell electrochemical reactions, there is very little actual *experimental* evidence for the role of TPBs in PEM fuel cells. In this report, a first ever detailed systematic study of the Air/Platinum/Nafion triple phase boundary is described, which attempts to elucidate the true nature, electrochemical properties, and scaling characteristics of TPBs in PEM fuel cell environments.

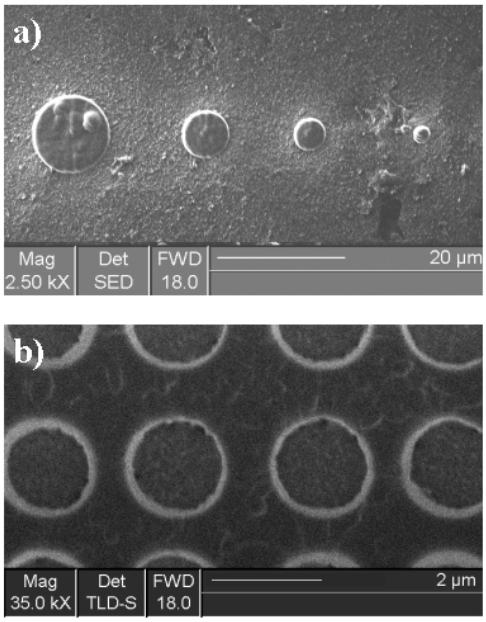

Figure 3: a) Electron micrograph of a series of Pt-microelectrodes directly patterned via FIB onto the surface of a Nafion membrane "half-cell" MEA. **b)** Higher magnification electron micrograph of a portion of an FIB patterned array of 1µm radius Pt-microelectrodes. After array patterning is complete, the electrodes are electrically interconnected with a series of FIB deposited Pt wires (not shown).

The TPB investigation is accomplished via the fabrication and measurement of micro-sized, simplified fuel cell catalyst geometries, such as the disk-shaped catalyst features pictured in Fig. 3. The micro-scale platinum features pictured in Fig. 3 are fully functioning fuel cells. Truly *micro* fuel cells, they may in fact be some of the world's smallest PEMFCs ever evaluated. Fig. 4(a) shows the absolute I-V curves for three different circular fuel cells with radii varying from 10-40µm. The absolute performance of these tiny fuel cells is insignificant; note the small values for current. Not surprisingly, the larger the fuel cell, the greater absolute current it delivers. Fig. 4(b) reports the results from the same three circular Pt-structures, but now normalized by area; on an area-normalized basis these results argue that smaller fuel cells are better. Intriguingly, the I-V curves of the three fuel cells are roughly comparable if they are scaled relative to their circumferences, rather than their areas, as shown in Fig. 4(c).

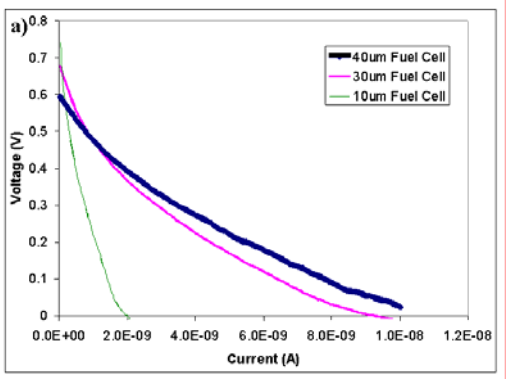

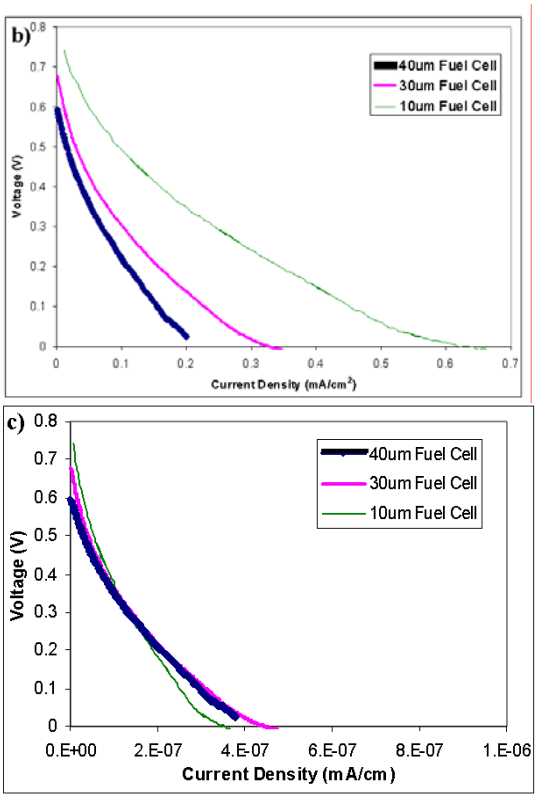

Figure 4: I-V curves for a series of Pt-microelectrodes operating as hydrogen-air fuel cells. (Heavy Line) 40µm radius microelectrode. (Medium Line) 30µm radius microelectrode. (Thin Line) 10µm radius microelectrode. **a)** Absolute current vs. voltage. **b)** Current density vs. voltage. **c)** Perimeter normalized current density vs. voltage.

In order to understand this scaling phenomenon, it is necessary to consider the fundamental electrochemical characteristics of the Pt-catalyst structures. A systematic impedance study allows us to separate the contributions of electrolyte resistance (R_e) and Faradaic impedance (R_f) of the oxygen reduction reaction (ORR). The results of this study are given in figures 5(a) and 5(b). As Fig. 5(a) reveals, R_e for the Pt-electrode structures is proportional to r^{-2} for large area electrodes and proportional to r^{-1} for small area electrodes. For small electrodes (when the electrode size, r, is much smaller than the electrolyte thickness, t) the measured electrolyte resistance, R_e, can be shown to be inversely proportional to the electrode radius[33]:

$$R_e = \frac{\rho}{4r}, \quad r << t \qquad (1)$$

Whereas for r>>t, the resistance is inversely proportional to the electrode area:

$$R_e = \frac{\rho * t}{\pi r^2}, \quad r >> t \qquad (2)$$

Thus, Fig. 5(a) relates a purely geometrical effect owing to the transition from an area-related electrolyte resistance for r>>t, to a point contact dominated spreading resistance for r<<t. This transition is recovered in the results of a simple finite element simulation (Fig. 6). In fact, the Nafion properties can be extracted by fitting the data to the simple finite element simulation, as shown by the dotted line in Fig. 5(a). A

parametric best fit of the finite element simulation to the experimental data is obtained for simulation values of Nafion thickness t=90μm and Nafion resistivity ρ=3000Ωcm. (Nominal reference values for dry Nafion 115 are t=125μm, ρ=10-100Ωcm.[34-36]) Since the electrolyte in our experiments is subjected to a desiccating high vacuum environment prior to electrochemical measurement, it is unsurprising that our experimentally fit resistivity values are high.

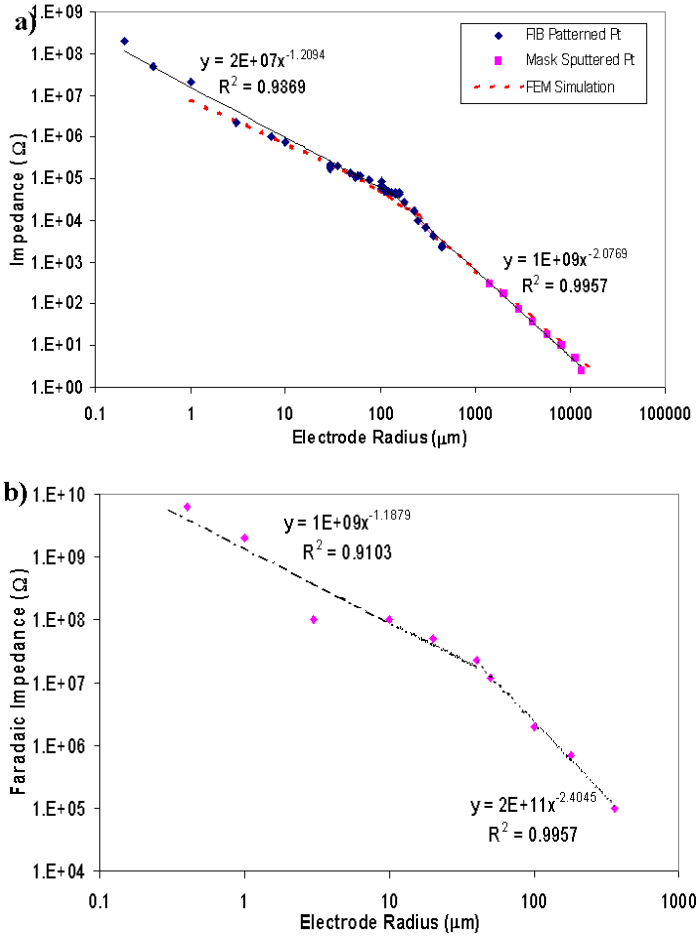

Figure 5: a) Electrolyte impedance (R_e) vs. Pt-microelectrode radius. (♦) Experimental data from FIB patterned Pt-microelectrodes. (■) Experimental data from large-area shadow mask sputtered Pt electrodes. (---) Model fit based on finite element simulation. Solid lines and equations show slope ≈ 1 for (r < 100μm), slope ≈ 2 for (r > 100μm) **b)** Faradic impedance (R_f) vs. electrode radius. (♦) Experimental data from FIB patterned Pt-microelectrodes. Dashed lines and equations show slope ≈ 1 for (r < 40μm), slope ≈ 2 for (r > 40μm)

Perhaps more surprising are the results in Fig. 5(b), which show that R_f is also roughly proportional to r^{-2} for large electrodes and proportional to r^{-1} for small electrodes. Note first that the Faradaic impedance is several orders of magnitude larger than the electrolyte impedance. This indicates that R_f for the ORR dominates the electrochemical behavior of these circular micro fuel cells. (The losses from R_e are negligible in comparison.)

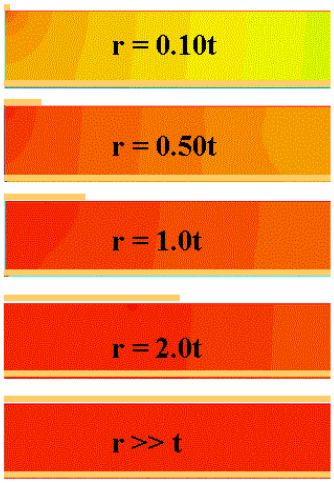

Figure 6: Field simulation results from the finite element model showing the transition from spreading resistance dominance for r << t to a uniform-field area-based resistance for r >> t.

For electrodes smaller than about 40μm, we see a direct relation between Pt-microelectrode circumference and R_f. This expected result indicates that the ORR kinetics are scaling with the length of the TPB. As hypothesized earlier, the 2μm thickness of the catalyst structures prevents the bulk of the electrode area from participating in the ORR process. Instead, only the perimeter participates as active TPB for the Faradaic reaction. Interestingly, for microelectrodes greater than 40μm, the ORR kinetics no longer scale with a circumferential based TPB length. The roughly r^{-2} dependence for the larger Pt-electrodes is believed to arise from a cracking process due to the dimensional instability of the Nafion electrolyte. Post-mortem electron microscope analysis of Pt-microelectrodes confirms that cracking typically occurs for electrodes greater than about 40μm. (See Fig. 7)

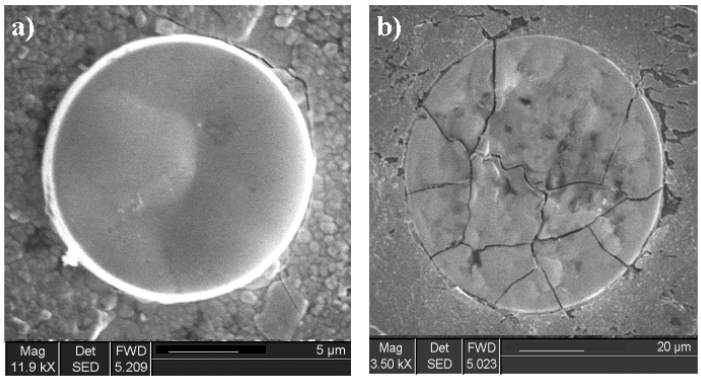

Figure 7: a) A typical 10μm radius FIB patterned Pt-microelectrode imaged after testing under ambient conditions. Despite the vacuum-ambient-vacuum cycling the microelectrode remains intact. **b)** A typical 40μm radius FIB patterned Pt-microelectrode imaged after testing under ambient conditions. After the vacuum-ambient-vacuum cycling the microelectrode exhibits cracking.

The cracking is believed to be due to the expansion of the Nafion electrolyte upon removal from the vacuum environment and exposure to ambient humidity. This area distributed cracking introduces additional TPB sites in the larger electrode structures, which should scale roughly proportional to electrode area. For Pt-electrodes smaller than 30μm, no cracking is observed. For these small, unblemished electrodes, then, it is possible to extract a Faradaic resistance per unit TPB length (R_{TPB}). R_{TPB} is calculated as:

$$R_{TPB} = 2\pi r * R_f \qquad (3)$$

From the data in Fig. 5(b), R_{TPB} can be estimated at roughly $R_{TPB} = 6*10^9$ Ωμm.

As noted earlier, the Faradaic impedance dominates the electrochemical behavior of these micron-sized catalyst structures ($R_f >> R_e$). Thus, catalyst structures with an increased TPB length per unit area should show proportionally improved electrocatalytic performance. In Fig. 8, a uniform 40μm x 40μm square electrode is compared to a sectioned 40μm x 40μm square electrode. The two electrodes have the same total Pt area, but the sectioned electrode has 5 times greater TPB length. (Each interior section contributes 2 lengths of TPB.) As the impedance spectra for the two structures clearly show, the Faradaic resistance of the sectioned electrode is about 1/5 that of the uniform electrode. Not only do the Faradaic impedances for the two structures scale qualitatively as predicted, but the absolute quantitative values for the two structures scale almost exactly as predicted using the previously determined Faradaic resistance per unit TPB length, $R_{TPB} = 6*10^9$ Ωμm. This result grants at least some confidence that the TPB properties derived from the circular microelectrodes can be used for other geometries.

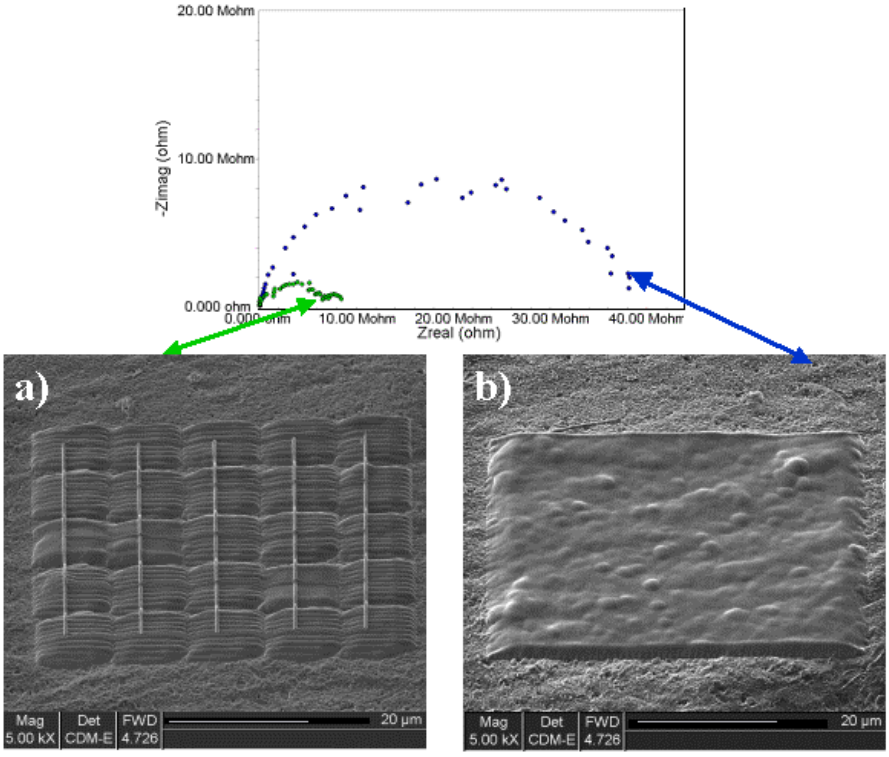

Figure 8: EIS Nyquist spectra and corresponding micrographs for two FIB patterned 'artificial Pt-catalyst microstructures' showing the direct relation between faradic impedance and TPB length. **a)** 40μm square Pt-catalyst structure sectioned into 25

separate 8μm x 8μm squares. Electrical contact between the 25 sections is assured by the Pt interconnect wires. The sectioned structure shows a Faradaic impedance of around 8 MΩ. **b)** Undivided 40μm square Pt-catalyst structure. This undivided electrode shows a Faradaic impedance of around 40 MΩ. The two electrodes are imaged at a 53^{o} angle, thus because of foreshortening they do not appear square.

Having determined a quantitative value for the resistance per Pt/Nafion triple phase boundary length, we can also infer TPB density requirements for a high performance PEMFC. For most fuel cell requirements, a cathodic ORR resistance of around 0.15Ωcm^2 is acceptable[37]. This implies a TPB density on the order of 10^6 cm/cm^2. Assuming plane packed spherical platinum particles, each of which contributes an average TPB on the order of its projected circumferential length, this suggests an average catalyst particle size smaller than 30 nm is necessary to achieve the required ORR resistance.

AFM Impedance Imaging

The hope of an AFM impedance imaging system is the ability to directly visualize and correlate relationships between microstructure and performance for fuel cells and other alternative energy conversion devices at the sub-micron length scale. While this is the ultimate goal, intermediate proof of the 2D AFM impedance-imaging concept has first been demonstrated using specially developed micro-scale gold test patterns. (Experimental configuration follows Fig. 2b.) Representative impedance modulus (Z_0) and impedance phase (θ) images obtained from the test patterns are compared to their topographic counterparts (topography deflection images) in Fig. 9. Note that the phase angle for the gold region is close to zero, indicative of ohmic transport, while the phase of nitride is close to –90^{o}, indicative of capacitive behavior. (Mean phase values for the gold and nitride regions are -0.09^{o} and -88^{o}, respectively.) Note that at the 1μm scale, the boundary between the nitride film and the gold is more clearly resolved by the impedance image than the topography image. Full impedance spectra taken at several points on the sample (points A-E in Fig. 9) confirm the ohmic response of the gold and the capacitive behavior of the nitride (Fig. 10).

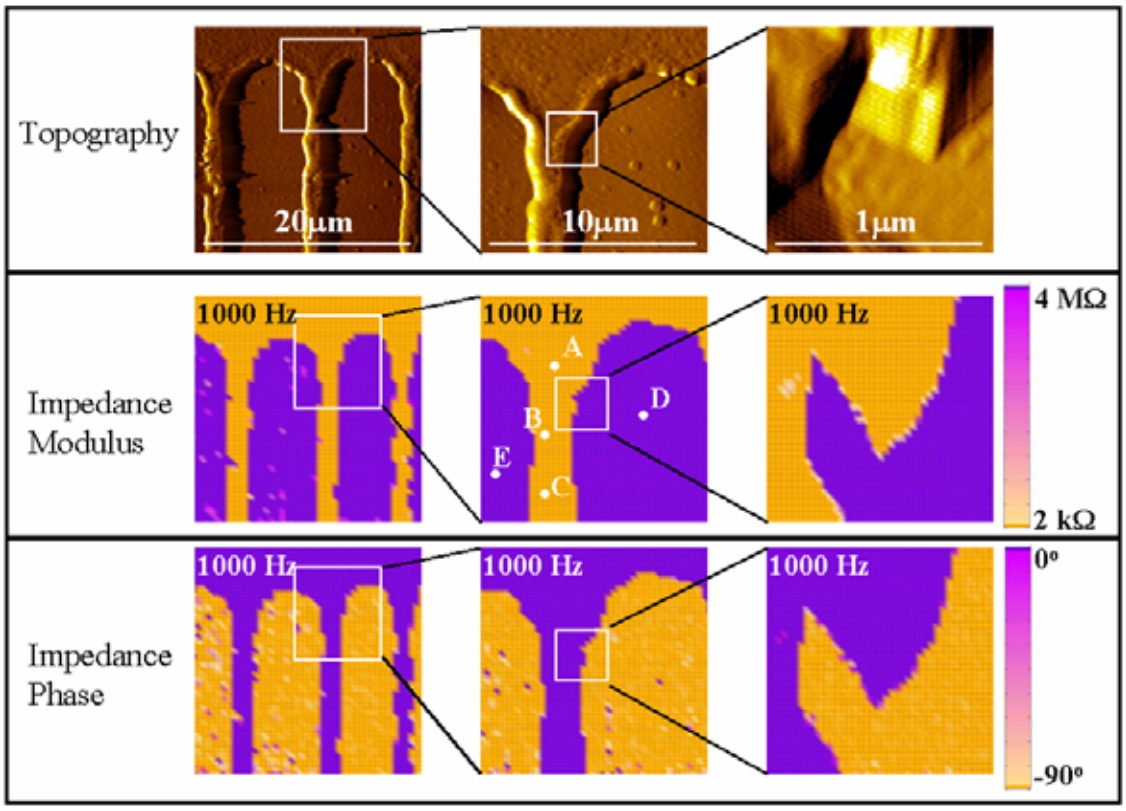

Figure 9: Topograhphic deflection (top row), Impedance modulus (middle row) and Impedance phase (bottom row) images from a gold/silicon nitride test pattern. Images increase in magnification from left to right. Images acquired according to the experimental configuration from Fig. 2b). Topographic deflection at 2Hz scan speed, 512 x 512 resolution. Impedance modulus and phase acquired at 1000 Hz, with a 10 mV excitation signal and 0V DC bias.

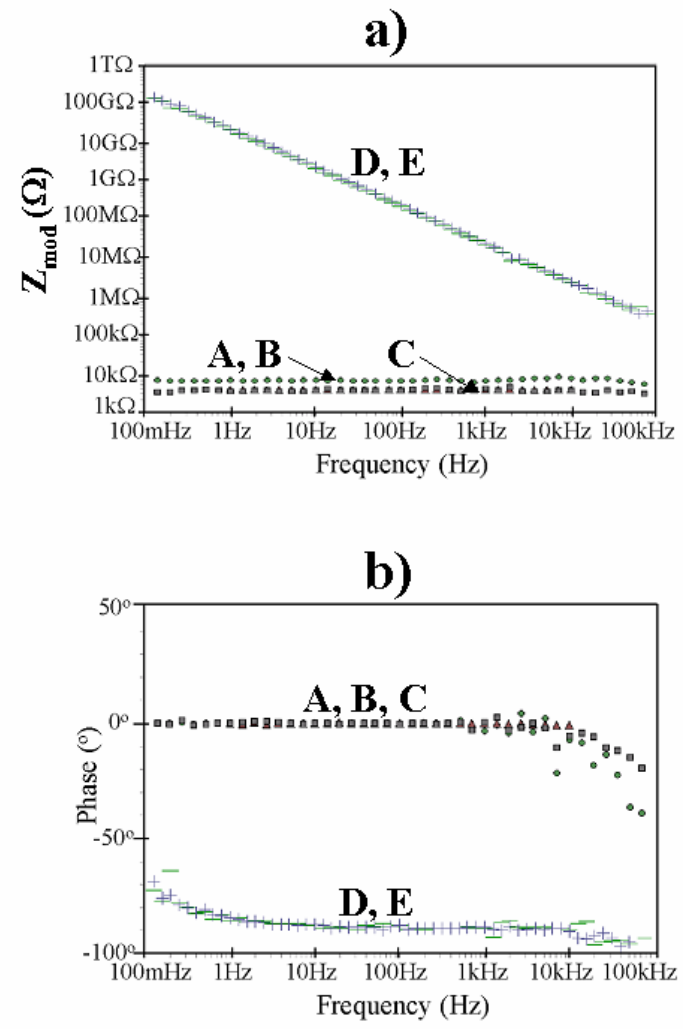

Figure 10: a) Bode impedance modulus spectra and **b)** Impedance phase spectra acquired at specific locations (A-E) on the gold/nitride test pattern. The measurement locations (A-E) are denoted on the 10 μm impedance modulus image in Fig. 9. Spectra from the gold film show ohmic behavior, while spectra from the nitride region show a capacitive response. The impedance spectra were acquired from 100kHz-100mHz with a 10 mV excitation signal and 0V DC bias.

As indicated by the color-scale, the impedance images in Fig. 9 show an apparent binary contrast between the gold and the nitride. The mean impedance of the gold is around 5000Ω, while the mean impedance of the nitride is $4*10^6$Ω. If the image contrast is adjusted so that variations at the low-end of the impedance range are visible, (Fig. 11a) further detail is resolved. Slight impedance variations, possibly due to changes in the thickness and topography of the gold film at the boundary with the nitride region, are apparent. Similar contrast adjustments at the high-end of the impedance range allow variations in the nitride film to be seen (Fig. 11b). The true impedance of the nitride film exceeds the measurement capabilities of our instrument at 1 kHz. Therefore, it is believed that these apparent variations in the nitride film impedance are simply a visualization of the error and noise structure of the instrument.

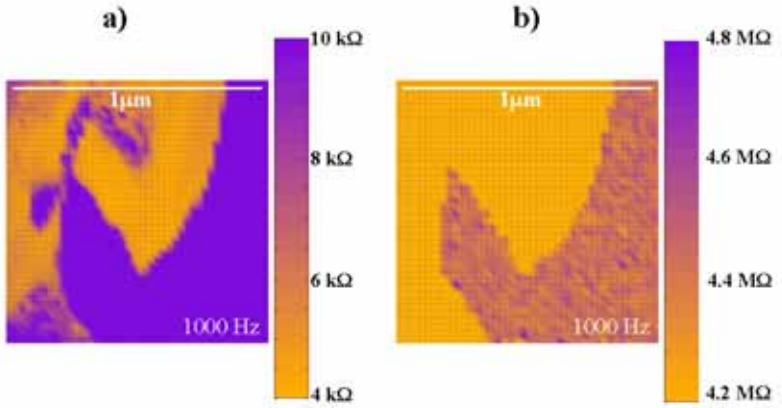

Figure 11: a) Impedance modulus image from a 1μm area of the gold/nitride test pattern, scale adjusted to show the contrast details in the gold film impedance. **b)** The same impedance modulus image scale adjusted to bring out the contrast details in the nitride film impedance. The apparent nitride film details are likely associated with the noise structure of the instrument. Images acquired at 1 kHz with a 10 mV excitation signal and 0V DC bias.

A practical example of AFM impedance imaging in the electronic domain is provided by a study of grain/grain boundary transport in commercial polycrystalline ZnO varistors. Following Fig. 2a), the impedance of a cross-sectioned commercial ZnO varistor was probed laterally between the AFM tip and a bulk top electrode. Thus, in addition to the local impedance response at the AFM tip, non-local impedance contributions from any intervening grain boundaries between the tip and the bulk electrode are also probed.

Coupled SEM, AFM topography deflection, and AFM Z_0 images from a 50μm region of the ZnO varistor are shown in Fig. 12. The Z_0 image was acquired with a 100mV excitation signal under +5V DC bias at 1 kHz. Several distinct ZnO grains are visible in the images. The ZnO grains at the upper left of the image show purely ohmic behavior at a +5V DC bias. These grains are closest to the bulk top electrode, which was positioned approximately 30μm above and to the left of the image field of view.

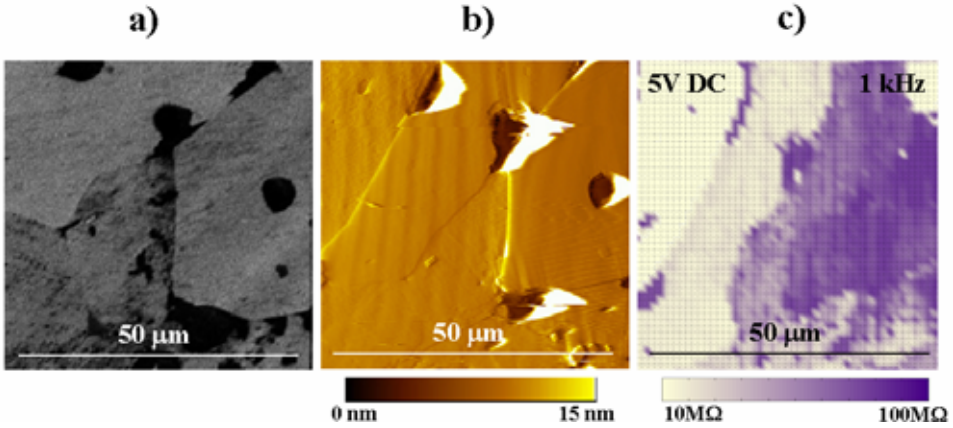

Figure 12: a) SEM image of a 50μm region of a polished, cross-sectioned commercial ZnO varistor. **b)** AFM topography deflection image of the same 50μm region, acquired at 2Hz scan speed, 512 x 512 pixel resolution. **c)** Impedance modulus image of the same

50μm region acquired according to the experimental configuration in Fig. 2a). Impedance modulus image data were acquired at 1 kHz with a 100 mV excitation signal and 5V DC bias. The bulk electrode for this measurement is located approximately 30μm above and to the left of the image field of view.

The highly nonlinear IV properties of ZnO varistors arise from double-Schottky like barriers formed at the grain boundaries of the material. Below a critical grain-boundary breakdown voltage (typically 3-4 volts), transport across the boundary is almost purely capacitive and the boundary is highly insulating. Above the critical voltage, however, transport across the grain boundary becomes ohmic.[38,39]

Fig. 13 shows a set of Z_0 and θ images for the same 50μm area at five different bias voltages ranging from 0V DC to +8V DC. (Measurements acquired at 1 kHz with a 100mV excitation.) Note how individual grain boundary barriers are shorted one by one during the DC bias voltage ramp, starting from the upper left with the grains closest to the electrode. This grain-by-grain cascade visibly demonstrates the highly nonlinear IV characteristics of the polycrystalline varistor. The first grains to exhibit ohmic transport characteristics do so at 3-4 V DC, indicating that they are removed by a single grain boundary from the top electrode. The other grains become ohmic between 5-8 V DC, indicating that they are probably separated by two grain boundaries from the top electrode. This result is reasonable given the varistor's 40μm average grain size and the location of the top electrode 30μm above and to the left of the images.

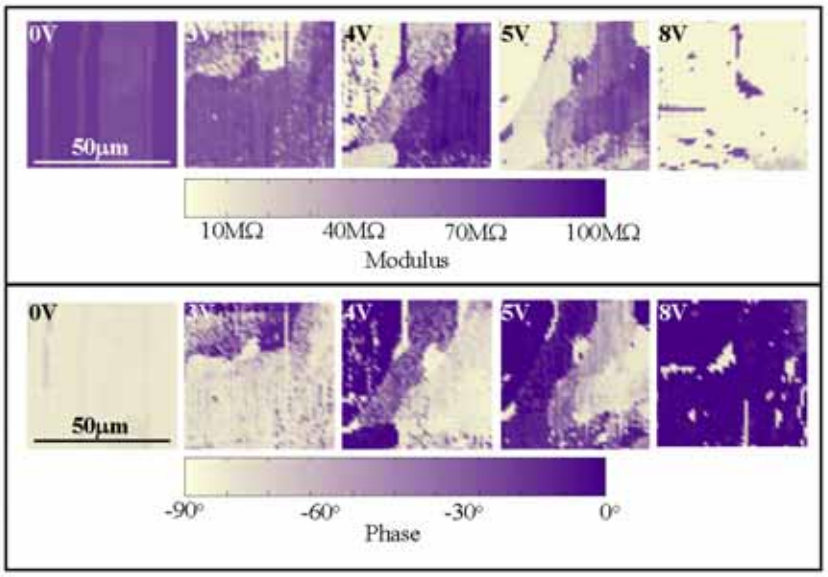

Figure 13: Impedance modulus (top row) and impedance phase (bottom row) images measured as a function of DC bias for the same 50μm ZnO region documented in Fig. 12. From left to right, the images are acquired with increasing DC bias; 0V, 3V, 4V, 5V, 8V. All images acquired at 1 kHz with a 100 mV excitation signal. Note the grain-by-grain "cascade" with increasing DC bias as the grains become conductive, starting with the grains on the upper left closest to the bulk electrode.

Fig. 14 presents Z_0 and θ images as a function of measurement frequency for the same 50μm area explored in Fig. 12 and 13. (Measurements acquired at +4V DC bias with a 100mV excitation.) Note the improved impedance contrast at lower frequency. This contrast improvement is expected based on an analysis of the RC-impedance behavior of the varistor grains. In single-frequency impedance imaging, careful choice of the imaging frequency based on the characteristic behavior of the analyzed system is necessary in order to achieve maximum impedance contrast. A theoretical treatment is intended for a later publication.

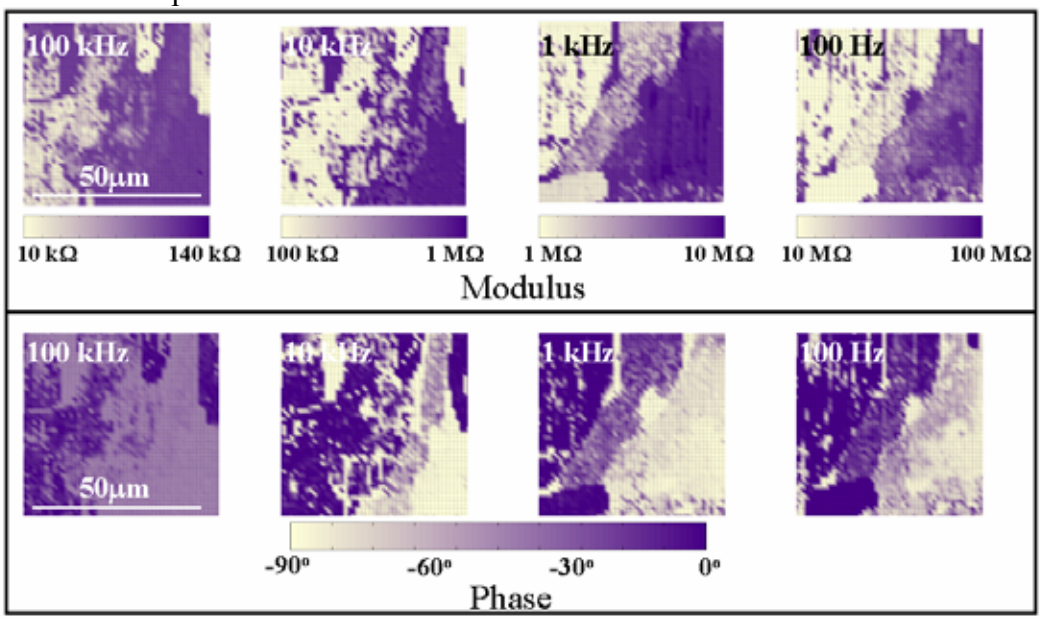

Figure 14: Impedance modulus (top row) and impedance phase (bottom row) images measured as a function of frequency for the same 50μm ZnO region documented in Fig. 12 and 13. From left to right, the images are acquired with decreasing measurement frequency; 100kHz, 10kHz, 1kHz, 100Hz. All images were acquired with a 100 mV excitation signal and 4V DC bias. Note the improved impedance contrast at lower frequency.

Fig.15 demonstrates the sub-micron resolution capabilities of the AFM impedance imaging technique with a series of "zoom-in" magnifications on a ZnO triple junction. The small triangular shaped region at the junction between the three ZnO grains (clearly visible in the 6μm image) is a Bi_2O_3 second-phase inclusion. (Confirmed by EDAX analysis.) Bi_2O_3 is added to ZnO varistors to control the grain-boundary properties of the material. Excess Bi_2O_3 typically phase-segregates to the ZnO triple junctions. It is non-conductive.

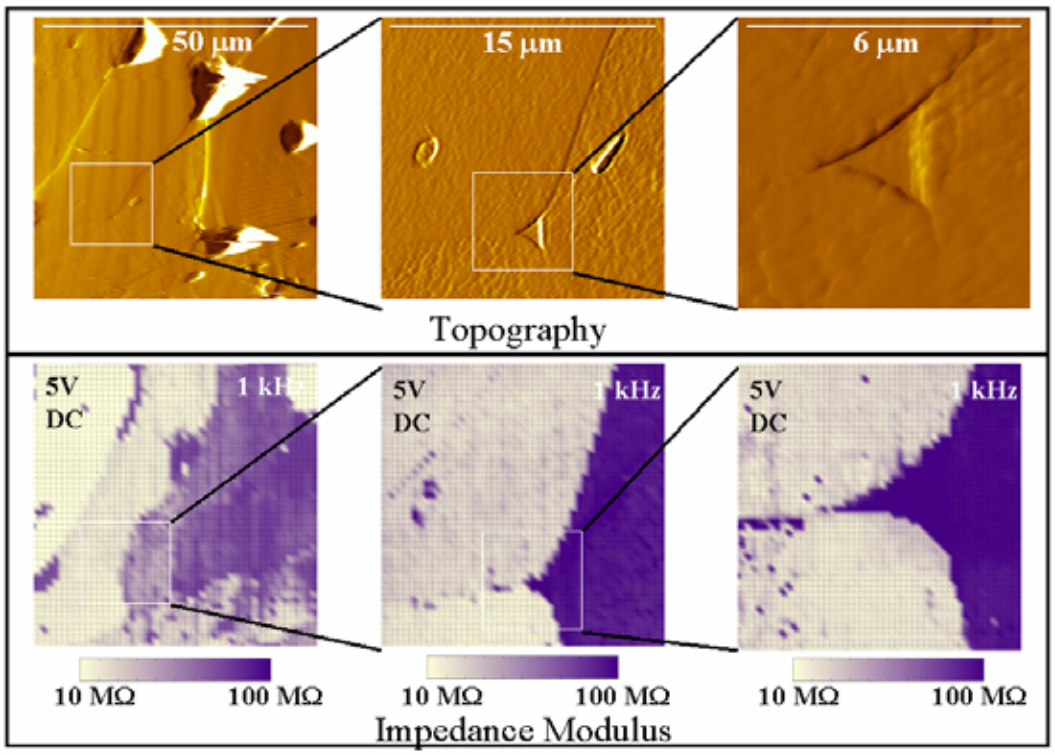

Figure 15: AFM topography deflection (top row) and impedance modulus (bottom row) images, increasing in magnification from left to right. (50µm, 15µm, and 6µm scan regions, respectively.) Impedance-modulus images are acquired at 1 kHz with a 100 mV excitation signal and 5V DC bias. The images "zoom" into a triple-junction region between 3 ZnO grains. The V-like intrusion between the 3 grains is a highly insulating Bi_2O_3 second phase inclusion. (Confirmed by EDX analysis.)

In addition to single-frequency impedance images, full impedance spectra can be acquired at specified locations on a sample. Fig. 16 compares impedance spectra acquired at several distinct locations on the varistor sample. Locations a) and b) are within ZnO grains, and show a transition from capacitive, blocked behavior at low DC bias to ohmic, conductive behavior at high DC bias. Location c) is inside a second phase Bi_2O_3 inclusion, and shows insulating behavior over the entire DC bias range.

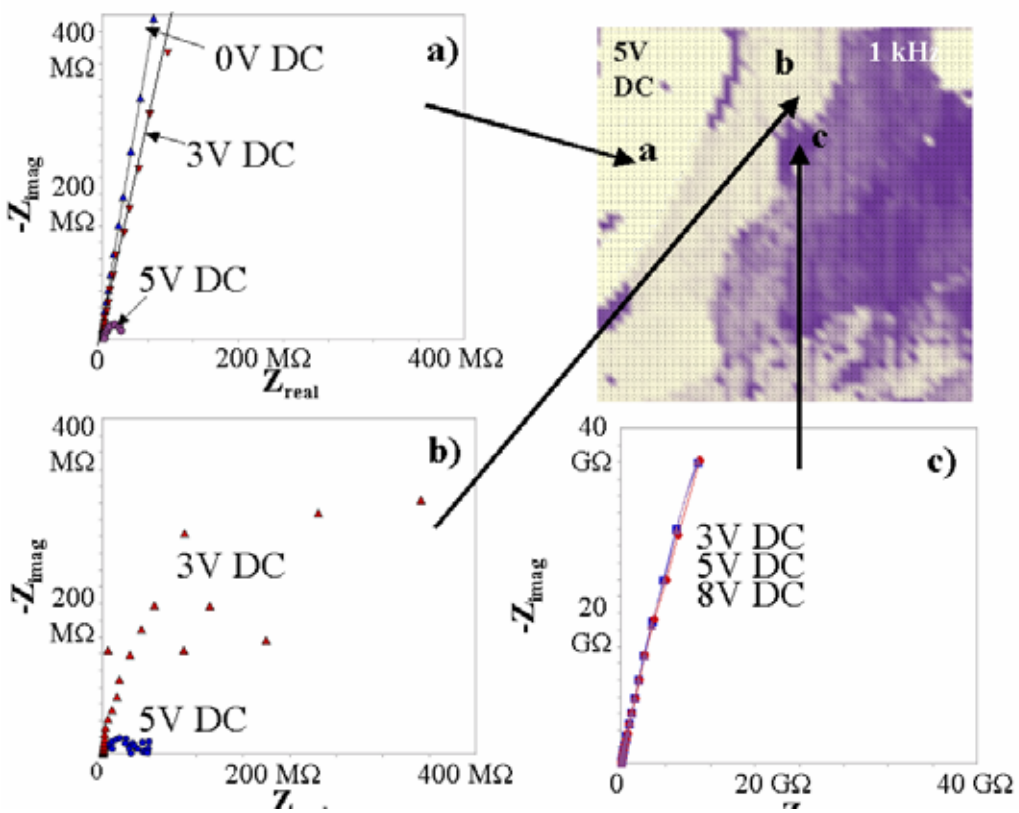

Figure 16: Impedance spectra (Nyquist format) from various locations on the ZnO-sample surface. **a)** Impedance spectra vs. DC bias acquired at location **a**. Capacitive blocking behavior is seen for 0V and 3V applied DC bias. At 5V applied DC bias, an impedance loop develops. **b)** Similar impedance behavior vs. DC bias is observed at location **b** on the sample surface. **c)** At location **c**, capacitive behavior is observed at all levels of applied DC bias. Location **c** corresponds to a Bi_2O_3 second phase inclusion.

The AFM impedance technique may also be applied to studies of ionic materials and/or electrochemical systems. In this next section, we report localized impedance measurements on the protonated form of Nafion solid polymer electrolyte.

Following the experimental setup in Fig. 2c, a platinum coated AFM tip is used as a local probe of the proton (H_3O^+) density in a Nafion 117 membrane. (30 nm Pt sputtered over the standard conductive diamond AFM tip.) Hydrogen gas is provisioned to a sealed anode compartment underneath the electrolyte membrane sample, providing a continuous supply of protons into the membrane. (The anode is a standard polymer-electrolyte fuel cell catalyst-electrode, details given elsewhere.[40,41]) Applying a DC bias to the platinum-coated AFM tip (the bias is applied relative to the anode electrode, which is pseudo-reversible because of its much larger size) causes a Faradaic charge transfer reaction to occur, with protons from the membrane combining with oxygen from the air to produce water. Essentially, the Pt-coated AFM tip, in contact with the electrolyte membrane, becomes a tiny, moveable, fuel cell cathode. The kinetics of the cathode reaction will be proportional to the local concentration of protons in the membrane. Using

the AFM-impedance technique to probe this Faradaic charge transfer reaction permits the local activity of the electrolyte membrane to be visualized.

The impedance spectra in Fig. 17 confirm the ability of the Pt-coated AFM tip to act as a localized electrochemical probe. A Faradaic-like charge transfer loop is seen in the impedance response only if all of the following conditions are met:

1) A Pt-coated tip is used
2) H_2 gas is provisioned to the anode compartment
3) A cathodic DC bias is applied
4) The tip is in hard physical contact with the electrolyte membrane

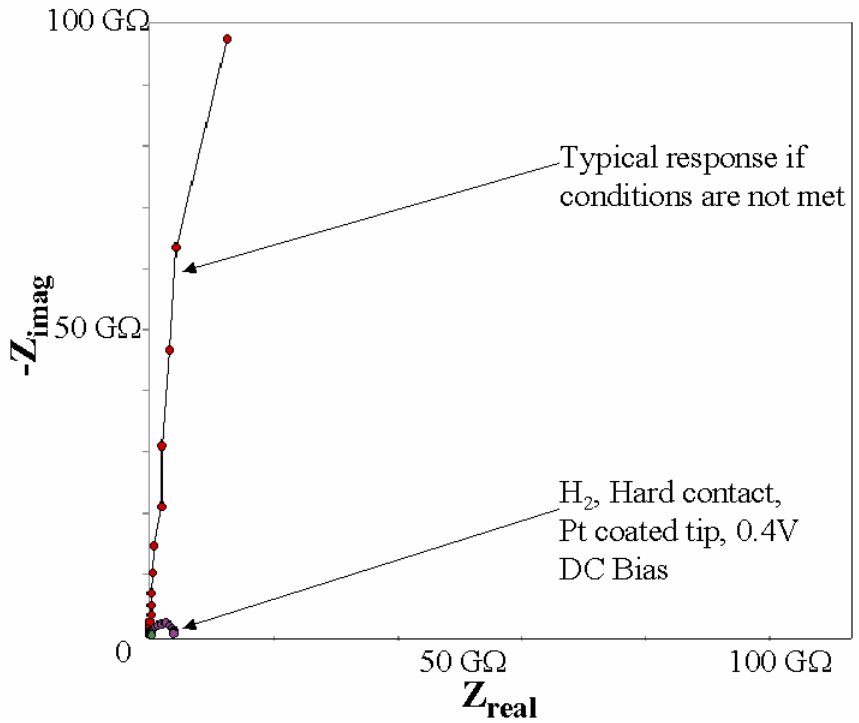

Figure 17: Representative Nyquist impedance spectra for localized AFM impedance measurements on Nafion membrane. Impedance spectra are measured according to the experimental configuration in Fig. 2c) over the frequency range 100kHz to 100mHz with a 30 mV excitation signal. An impedance loop appears only when H_2 gas is provisioned to the anode, the AFM tip is in hard contact with the membrane, the AFM is coated with platinum, and a cathodic DC bias is applied to the tip. If any combination of the above conditions in not met, purely capacitive blocking behavior is observed instead. These observations suggest that the impedance loop behavior arises from a Faradaic charge transfer reaction occurring at the tip/electrolyte membrane interface.

Observation of this response only when all 4 conditions are met indicates that the loop most likely corresponds to a Faradaic reaction at the tip-electrolyte interface. This conclusion is supported by the behavior of the impedance loop with applied DC bias, as shown in Fig. 18. The loop shrinks with increasing DC bias, highly characteristic of a Faradaic charge-transfer reaction.

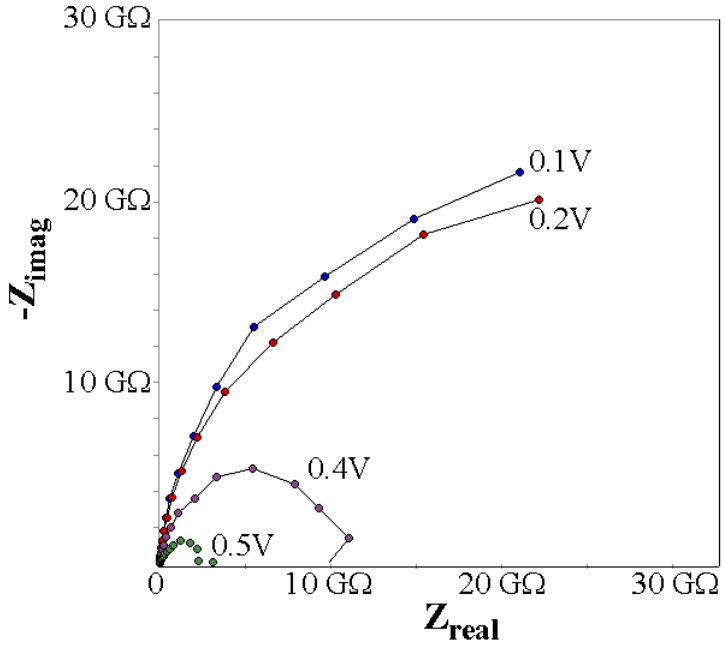

Figure 18: Nyquist spectra of the Pt-tip/Nafion impedance response as a function of applied DC bias. Impedance spectra are measured according to the experimental configuration in Fig. 2c) over the frequency range 100kHz to 100mHz with a 30 mV excitation signal. H_2 gas is provisioned to the anode, the AFM tip is in hard contact with the membrane, and the AFM is coated with platinum. The impedance loop shrinks with increasing DC bias, characteristic of a Faradaic charge transfer process.

Translation of the AFM tip across the surface of the electrolyte permits spatially resolved "electrochemical" impedance images to be acquired, just as electrical impedance images were acquired for the gold patterns and the ZnO varistors. Fig. 19 shows sets of fixed-frequency AFM impedance images of a Nafion electrolyte membrane. These images were acquired at 1 Hz with a 30mV excitation signal, 0.4V DC cathodic bias (the bias favors the oxygen reduction reaction, thus decreasing the Faradaic charge transfer resistance and improving the signal to noise). The images compare the impedance response from a dry Nafion membrane (imaged under dry, 0% relative humidity, room temperature air) vs. the same area of the same membrane when hydrated (imaged under 30% relative humidity, room temperature air). The hydration level of the Nafion electrolyte significantly influences its solvated proton ($H_3O^+ \cdot nH_2O$) concentration and conductivity. This is readily apparent from the AFM impedance images, which show a dramatic change in the impedance response (note change in the impedance scale). The corresponding topography images are not shown, but bear no relation to the impedance response. Membrane swelling and consequent dimensional expansion prohibited measurement of the membrane under still higher humidity levels.

It is well known that Nafion is not a homogeneous material, but instead consists of hydrophilic and hydrophobic phase-segregated regions. The apparent features seen in the Nafion impedance images of Fig. 19 may correspond to hydrophilic domains in the membrane. The apparent sizes of these domains (refer to the 1μm image) are on the order of several hundred nanometers. This is larger than the 40-100 nm domains visualized by

a SSPM study of dry Nafion recently published by Kiyoshi et al.[42] Kiyoshi and co-workers' study looked at the variation in surface potential across a Nafion membrane. Several tens of high-surface potential spots were seen in a 10μm by 10μm scan of a Nafion membrane, and were attributed to hydrophilic water-containing regions in the Nafion electrolyte. The larger domain size in our results may be due to several factors, including drift, "smearing", and the possible existence of a water meniscus at the tip/sample contact. The images in Fig. 19 were acquired in a vertical scan-mode. A possible vertical distortion or "smearing" effect can be seen in the 1μm images. We hypothesize that water from the hydrophilic domains on the Nafion surface might be captured on the tip as it steps from point to point, resulting in an extension, or "smearing" of the apparent hydrophilic domain sizes, especially in the scan direction. The formation of a water meniscus at the tip/sample junction would also serve to increase the overall apparent size of the hydrophilic Nafion domains. Nevertheless, these qualitative results show an overall decrease in impedance and an expansion of the low-impedance domains with increasing hydration, which are consistent with current knowledge on the behavior of Nafion.

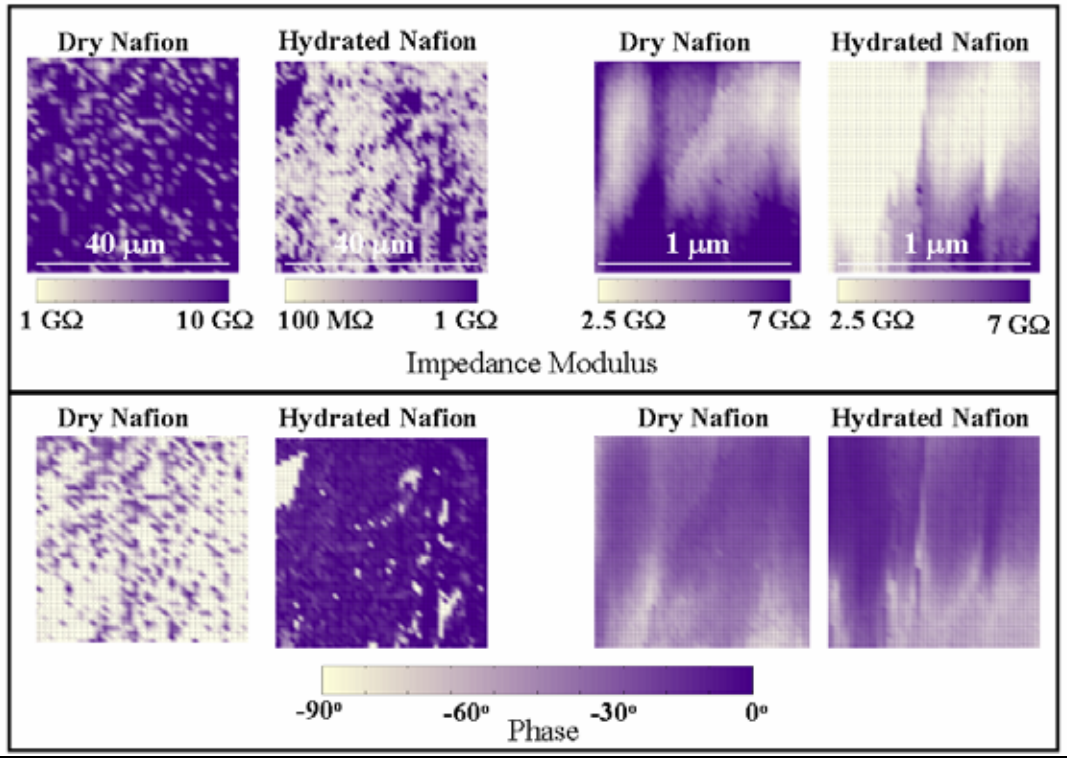

Figure 19: Impedance modulus (top row) and impedance phase (bottom row) images of the Nafion electrolyte membrane as a function of humidity. The image sets on the left compare the impedance response under dry (0% relative humidity) vs. ambient (30% relative humidity) conditions for a 40μm area of the Nafion membrane. The image sets on the right compare the impedance response under dry vs. ambient humidity conditions for a 1μm area of the Nafion membrane. Images acquired at 1 Hz with a 30mV excitation signal, 0.4V DC cathodic bias. The hydration level of the Nafion electrolyte significantly influences its H_3O^+ concentration and ionic conductivity, as is readily apparent from the impedance images (note change in the impedance modulus scale for the left image set).

Progress

By improving fuel cell efficiency and lowering fuel cell costs, researchers can remove major remaining barriers towards widespread fuel cell implementation. These goals can be achieved by improving both catalyst activity, and by improving electrolyte conductivity. The triple phase boundary studies and AFM-impedance measurement system described in this report provide valuable research and development tools to further explore catalyst activity and electrolyte conductivity. Implementation of these new R&D tools over the next several years can help pave the way towards greater scientific understanding of catalyst and electrolyte phenomena, eventually leading to better fuel cell systems.

The combination of Atomic Force Microscopy with Impedance Spectroscopy provides unique insights into electrochemical behavior of a variety of materials important for fuel cell development. In particular, we have been able to measure the catalytic performance of PEM fuel cells comprised of one or a few nano-scale platinum particles. Our experimental configuration allows studying cathodic overvoltage, which represents a key bottleneck in improving fuel cell efficiency and power density. We are currently exploring AFM Impedance Spectroscopy measurements for the study of space charge phenomena in Solid Oxide Fuel Cell membranes. We expect to visualize spatial variations of oxygen ion conductivity and study the benefits of introducing linear lattice defects such as dislocations for enhancing ionic conductivity in electrolyte materials as well as and mixed electronic ionic conductors for electrodes

Improvements in catalytic activity or increasing conductivity of electrode and electrolyte materials can substantially advance fuel cell power density and efficiency, a key performance metric for the practical use of fuel cells in cars.

Future Plans

The findings and techniques discussed in this report suggest many avenues for further research. Acknowledgement of the finite TPB width at Platinum/Nafion interfaces suggests new directions in catalyst layer design. Initial indications place the effective "TPB-width" on the order of many 10's to 100's of nanometers. This sets a target length scale for optimal catalyst layer nanostructures. It also suggests that novel planar-multilayered or intentionally patterned catalyst layers may prove effective.

The AFM impedance technique is ripe for application to many fields. To maximize the power and utility of the AFM impedance technique, further improvements in sensitivity, speed, and resolution should be investigated. Reduction of stray capacitance and other sources of spurious AC response can be achieved through careful tip design, thus allowing access to smaller RC time constants. The RC characteristics of the tip can be improved via selected area conductive patterning of the tip. Ideally, only the extreme end of the tip should be conductive, with only a small conductive pathway leading out to the measurement system. Further noise reduction and bandwidth improvement can be gained through tip shielding—for example with the development of innovative coaxial type tip geometries. Some of this exciting work is already ongoing by researchers around the world and by other members of our laboratory.[43,44]

Because the properties of an increasing number of materials depend strongly on nano-scale structure and processes, nano-scale characterization techniques such as AFM-impedance imaging are likely to be increasingly useful. Possible applications include solid electrolytes, semiconductors, solar cells, electro ceramics, coatings and corrosion research, and Li-ion battery and fuel cell systems. Localized AC impedance and transient potential techniques may be especially critical in the domain of electrochemical systems. Faradaic reactions, ionic transport and diffusion are best studied with transient techniques, making AFM impedance measurement extremely attractive for these applications.

Publications

1. R. O'Hayre and F. B. Prinz, The air/platinum/Nafion triple phase boundary: characteristics, scaling, and implications for fuel cells. J. Electrochem. Soc., **151**, A756, (2004)
2. R. O'Hayre, M. Lee, and F. B. Prinz, Ionic and Electronic Impedance Imaging Using Atomic Force Microscopy. J. Appl. Phys. (in press)
3. R. O'Hayre, G. Feng, W.D. Nix, F.B. Prinz, Quantitative Impedance Measurement Using Atomic Force Microscopy. J. Appl. Phys. (submitted)
4. R. O'Hayre, Micro Scale Electrochemistry: Application to Fuel Cells, Ph.D. Thesis, Stanford University, Dept. of Materials Science and Engineering, May, 2004.
5. R. O'Hayre, M. Lee, and F. B. Prinz, Development of a nano-scale scanning impedance microscopy system, Oral presentation at the 203rd Meeting of the Electrochemical Society, Paris, France, April 27-May2, 2003.

References

1. M. Dresselhaus (Chair), Report of the basic energy sciences workshop on hydrogen production, storage, and use. Technical report, (2003)
2. M. S. Wilson and S. Gottesfeld, J. Appl. Electrochem., **22**, 1 (1992)
3. B.C.H. Steele, J. Mat. Sci., **36**, 1053, (2001)
4. J. Mizusaki, H. Tagawa, K. Tsuneyoshi, and A. Sawata, J. Electrochem. Soc., **138**, 1867 (1991)
5. A. Bieberle, L.P. Meier, and L.J. Gauckler, J. Electrochem. Soc., **148**, A646, (2001)
6. Kleitz and F. Petitbon, Solid State Ionics, **92**, 65, (1996)
7. V. Brichzin, J. Fleig, H.U. Habermeier, G. Cristiani, and J. Maier, Solid State Ionics, **152**, 499, (2002)
8. J. Fleig, J. Power. Sources, **125**, 228, (2002)
9. R. O'Hayre and F. B. Prinz, J. Electrochem. Soc., **151**, A756, (2004)
10. J. Fleig, J. Maier, Solid State Ionics, **85**, 9 (1996)
11. J. Fleig, S. Rodewald, J. Maier, Solid State Ionics, **136**, 905 (2000)
12. R. S. Lillard, P. J. Moran, H. S. Issacs, J. Electrochem. Soc., **139**, 1007 (1992)
13. F. Zou, D. Thierry, H. S. Issacs, J. Electrochem. Soc., **144**, 1957 (1997)
14. E. Bayet, F. Huet, M. Keddam, K. Ogle, H. Takenouti, J. Electrochem. Soc., **144**, L87 (1997)
15. M. Pilaski, T. Hammelmann, A. Moehring, M. M. Lohrengel, Electrochim. Acta, **47**, 2127 (2002)
16. P. De Wolf, J. Snauwaert, L. Hellemans, T. Clarysse, W. Vandervorst, M. D'Olieslaeger, D. Quaeyhaegens, J. Vac. Sci. Technol. A, **13**, 1699 (1995)
17. A. C. Diebold, M. R. Kump, J. J. Kopanski, D. G. Seiler, Proc. Electrochem. Soc., **94**, 78 (1994)
18. P. De Wolf, M. Geva, T. Hantschel, W. Vandervorst, R. B. Bylsma, Appl. Phys. Lett., **73**, 2155 (1999)
19. T. W. Kelley, E. L. Granstrom, C. D. Frisbie, Adv. Materials, **3**, 261 (1999)
20. A. Bietsch, M. A. Schneider, M. E. Welland, B. Michel, J. Vac. Sci. Technol. B, **18**, 1160 (2000)
21. M. Freitag, M. Radosavljevic, W. Clauss, A. T. Johnson, Phys. Rev. B, **62**, R2307 (2000)
22. S. J. Oshea, R. M. Atta, M. P. Murrell, M. E. Welland, J. Vac. Sci. Technol. B, **13**, 1945 (1995)
23. A Olbrich, B. Ebersbergerm C. Boit, Appl. Phys. Lett., **73**, 3114 (1998)
24. J. M. R. Weaver and D. W. Abraham, J. Vac. Sci. Technol. B, **9**, 1559 (1991)

25. M. Nonnenmacher, M. P. O'Boyle, H. K. Wickramasinghe, Appl. Phys. Lett., **58**, 2921 (1991)
26. C.C. Williams, W. P. Hough, S. A. Rishton, Appl. Phys. Lett., **55**, 203 (1989)
27. C.C. Williams, J. Slinkman, W. P. Hough, H. K. Wickramasinghe, Appl. Phys. Lett., **55**, 1662 (1989)
28. A. C. Diebold, M. R. Kump, J. J. Kopanski, D. G. Seiler, J. Vac. Sci. Technol. B, **14**, 196 (1996)
29. A. Layson, S. Gadad, D. Teeters, Electrochim. Acta, **48**, 2207 (2003)
30. S. Kalinin and D. A. Bonnell, Appl. Phys. Lett., **78**, 1306 (2001)
31. S. Kalinin and D. A. Bonnell, J. Appl. Phys., **91**, 832 (2002)
32. R. Shao, S.V. Kalinin, D.A. Bonnell, Appl. Phys. Lett., **82**, 1869 (2003)
33. J.W. Orton, P. Blood, The Electrical Characterization of Semiconductors, p. 53, Academic Press, London (1990)
34. T. Okada, S. MollerHolst, O. Gorseth, S. Kjelstrup, J Electroanal Chem, 442, 137 (1998)
35. T.A. Zawodzinski, C. Derouin, S. Radzinski, R. J. Sherman, V. T. Smith, T. E. Springer, S. Gottesfeld, J. Electrochem. Soc., 140, 1041 (1993)
36. K. D. Kreuer, Solid State Ionics, 97, 1 (1997)
37. B.C.H. Steele, Solid State Ionics, 86-88, 1223 (1996)
38. D.R. Clarke, J. Am. Ceram. Soc., **82**, 485 (1999)
39. R. Einzinger, Appl. of Surf. Sci., **3**, 390 (1979)
40. R. O'Hayre, F.B. Prinz, submitted, J. Electrochem. Soc.
41. S. Wilson, S. Gottesfeld, J. Appl. Electrochem., **22**, 1 (1992)
42. K. Kiyoshi, H. Morikawa, T. Umegaki, J. Electrochem. Soc., **150**, A193 (2003)
43. R. Fasching, Y. Tao, K. Hammerick and F. Prinz, Proc. SPIE 5116, Smart Sensors, Actuators, and MEMS, 128 (2003)
44. R. Fasching, Y. Tao and F. Prinz, Proc. SPIE 5341, Micromachining and Microfabrication Process Technology IX, 53, (2004)

Contacts

Fritz B. Prinz: fbp@cdr.stanford.edu
Ryan O'Hayre: rohayre@.stanford.edu
Minhwan Lee: piecoco@.stanford.edu